Electronic Supplementary Information

Solar Hydrogen Production Using Epitaxial SrTiO$_3$ on a GaAs Photovoltaic

L. Kornblum, D. P. Fenning, J. Faucher, J. Hwang, A. Boni, M.G. Han, M. D. Morales-Acosta, Y. Zhu, E. I. Altman, M. L. Lee, C. H. Ahn, F. J. Walker and Y. Shao-Horn

Experimental Methods

Solar Cell growth

GaAs solar cells are grown on on-axis 4-inch (001) p-GaAs wafers (~10^{19} cm^{-3}, AXT Inc.) by solid source molecular beam epitaxy (MBE) in a VEECO MOD GEN II chamber at a base pressure <10^{-10} Torr. Standard thermal sources are used to evaporate Al, Ga, Si and Be, whereas As$_2$ is evaporated using a thermally cracked source to produce dimer beam fluxes.

The GaAs substrates are degassed at 650°C (measured by pyrometry) for 30 min under As$_2$ overpressure. The substrate is then cooled to 600°C for III/V growth. GaAs is grown at 0.6 µm/hr with a V/III ratio of 15, while Al$_{0.4}$Ga$_{0.6}$As is grown at 1.0 µm/hr with a V/III ratio of 20. Si and Be are used as n- and p-type dopants, respectively. The reflectance high energy electron diffraction (RHEED) pattern transitioned from a spotty pattern to a streaky 2×4 pattern within 40 nm of GaAs growth, indicative of a smooth crystalline surface. Upon completion of the GaAs solar cell, the substrate is cooled to 300°C under an As$_2$ overpressure, during which time the RHEED pattern transitioned to a streaky centered 4×4 pattern. Upon reaching a substrate temperature of 300°C, the As$_2$ source is closed, and the substrate is cooled to room temperature. The As$_2$ source is then reopened for 90 min at substrate temperatures of 45-30°C resulting in an As protective cap layer, ~60 nm thick. The RHEED pattern became diffuse, indicating the presence of the amorphous As$_2$, within seconds of opening the As$_2$ source. The As-capped solar cell is then transferred in air to an oxide MBE chamber for subsequent epitaxial growth. The layers of the solar cell structure[39] are shown in Supplementary Table 1.

Cap	As_2		~60 nm
Emitter	n-GaAs	1×10^{18} cm^{-3}	100 nm
Base	p-GaAs	1×10^{17} cm^{-3}	2 µm
Buffer	p-GaAs	5×10^{18} cm^{-3}	20 nm
Reflector	p-$Al_{0.4}Ga_{0.6}As$	3×10^{18} cm^{-3}	50 nm
Buffer	p-GaAs	5×10^{18} cm^{-3}	250 nm
Substrate	p-GaAs	1×10^{19} cm^{-3}	600 µm

Supplementary Table 1. Structure of the GaAs solar cell that features a back surface field layer (BSF) [1].

np-GaAs junction photocathode operation

The operation of the np junction GaAs solar cell when used directly as a photocathode is illustrated using the schematic band diagrams in Supplementary Fig. 1. An electrolyte with a redox level matching the electron affinity of GaAs was chosen for simplicity. In the dark (Supplementary Fig. 1a), the junction is equilibrated and a built-in potential and field are formed across the depletion region, caused by the diffusion of carriers from both sides of the junction.[40] Under illumination (Supplementary Fig. 1b), photogenerated electrons and holes in and near the depletion region are separated by the built-in field and are the source of the photocurrent.[20] The populations of these excess carriers are represented by quasi-Fermi energy levels for electrons ($E_{F,n}$) and for holes ($E_{F,p}$), and their difference indicates the generated photovoltage.

a   p-GaAs   **b**   p-GaAs

electrolyte E_F electrolyte $E_{F,n}$ $E_{F,p}$

n$^+$-GaAs   n$^+$-GaAs
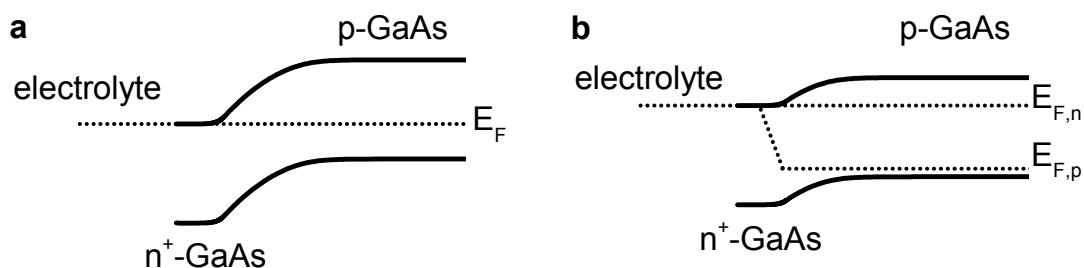
Supplementary Figure 1. Schematic band diagrams of the semiconductor solar cell showing the operation of the np junction solar cell under open-circuit conditions, **a**, in the dark and **b**, under illumination.

Dry photovoltaic cell characteristics without SrTiO$_3$ layer

Dry solar cell measurements are performed on GaAs solar cells with and without the SrTiO$_3$ layer. The GaAs devices without SrTiO$_3$ are fabricated by desorbing the As$_2$ cap in the same conditions as those used prior to SrTiO$_3$ deposition. 1x1mm^2 devices are fabricated using standard photolithography and wet etching. Device areas are defined by etching ~200 nm into the GaAs base using NH$_4$OH:H$_2$O$_2$:H$_2$O (2:1:50) to etch GaAs, and HF:HNO$_3$:H$_2$O (1:1:100) to etch through SrTiO$_3$ where applicable. Metal stacks consisting of Au/Ni/AuGe(/SrTiO$_3$) (100 nm/5 nm/100 nm) and Au/Cr(/SrTiO$_3$) (200 nm/20nm) are deposited by e-beam evaporation. Au/Cr is used for contacting the back of the wafers and for the top electrode for incident photon-to-current efficiency (IPCE) measurements. Current-voltage (J-V) measurements (Supplementary Fig. 2) are done with Au/Ni/AuGe top electrodes. J-V measurements show an open circuit voltage of 0.94 V and short circuit current of 14.3 mA/cm^2.
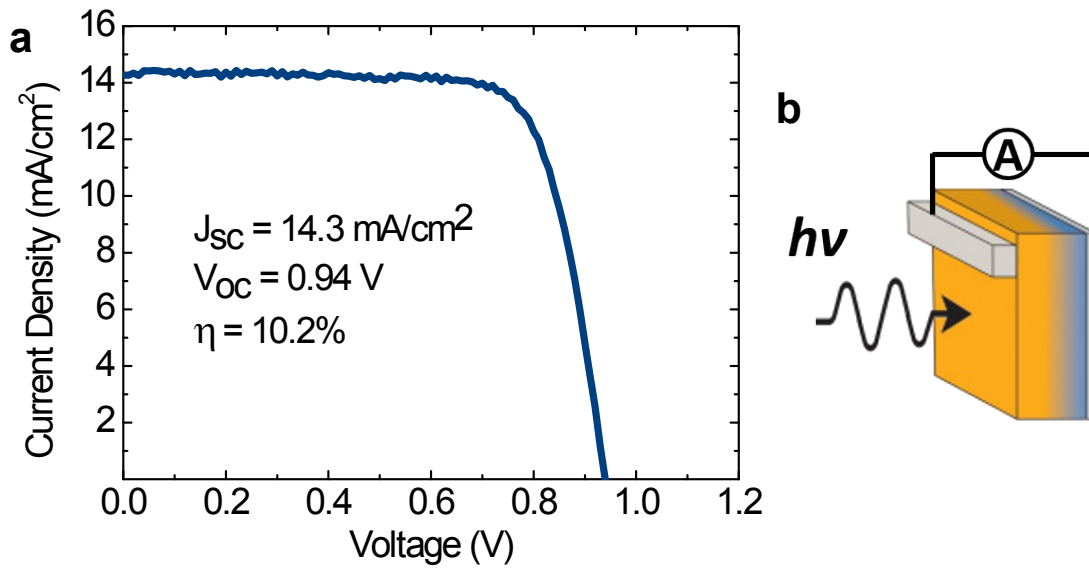
Supplementary Figure 2. a, Dry photovoltaic current-voltage curve of the solar cell described in Supplementary Table 1, without SrTiO$_3$. **b,** Schematic device structure for the dry measurements, with no oxide on the GaAs surface.

Molecular beam epitaxy of SrTiO$_3$

SrTiO$_3$ is grown 16 nm-thick on the GaAs solar cell structure described above (Supplementary Table 1) in a custom built MBE system by thermally evaporating 99.99% pure Sr (Sigma Aldrich) and Ti (Alfa Aesar) using effusion cells. High purity O$_2$ is introduced by a leak valve at an equilibrium pressure of 5~10×10^{-7} Torr. The substrate temperature is measured using a thermocouple in contact with a Si wafer placed behind the GaAs solar cell.

12×12 mm^2 pieces are cleaved from a 4 inch GaAs wafer and loaded into an oxide MBE chamber at a base pressure of $< 10^{-9}$ Torr. After arsenic desorption at 410°C, the growth is done using the process described by Droopad et al.,[27,41,42] with 0.5 monolayer (ML) of Ti metal deposited on the clean GaAs surface at 300°C, followed by 1 ML of SrTiO$_3$ deposited at a low O$_2$ background of $\sim 5 \times 10^{-7}$ Torr. The substrate is then annealed briefly at 500°C in vacuum. At this point, we introduce an additional step found to improve the nucleation of the crystalline oxide: 3 ML of SrTiO$_3$ are deposited at 375°C at the same O$_2$ background and then annealed in vacuum for 2 min at 640°C.[43] The same deposition and annealing conditions are then repeated for 5 ML of SrTiO$_3$. At this point the substrate is set to 500°C and SrTiO$_3$ is grown using codeposition at a higher background O$_2$ of $\sim 10^{-6}$ Torr. Once the growth is complete, the substrates are cooled down with an O$_2$ pressure of $\sim 10^{-6}$ Torr. X-ray diffraction (Rigaku Smartlab) demonstrates the high crystalline quality, as evident by the observation of finite-thickness oscillations around the (002) SrTiO$_3$ Bragg peak (Supplementary Fig. 3). A simplistic model is used to fit the data, assuming uniform properties throughout the SrTiO$_3$ layer. The asymmetry of the features and the disagreement with the data near $\sim 48°$ are attributed to strain distribution across the oxide. The strain is a consequence of $\sim -2.4\%$ in-plane lattice mismatch with the substrate and its distribution is attributed to the varying temperatures at different stages of the growth.

By growing the films thicker than 10 nm the resulting crystalline quality is improved. At first we were concerned that >10 nm thick oxides may increase carrier losses due to defect trapping and scattering, but as discussed earlier, we found that the key to robust charge transfer across the interface lays at the quality of the interface.

Scanning transmission electron microscopy (STEM) sample preparation is performed by focused ion beam with final Ga$^+$ ion energy of 5 keV. A 200 kV JEOL ARM 200CF equipped with a cold field-emission gun and double spherical-aberration correctors is used for high-angle annular dark field (HAADF) STEM image acquisition with a range of detection angles from 68 to 280 mrad (Fig. 1b). We note that some areas of the interface featured local defects; these defects grow under the TEM beam within tens of seconds of imaging. We therefore cannot rule out the existence of these defects in the original sample. An example of such defects is presented in Supplementary Fig. 4.
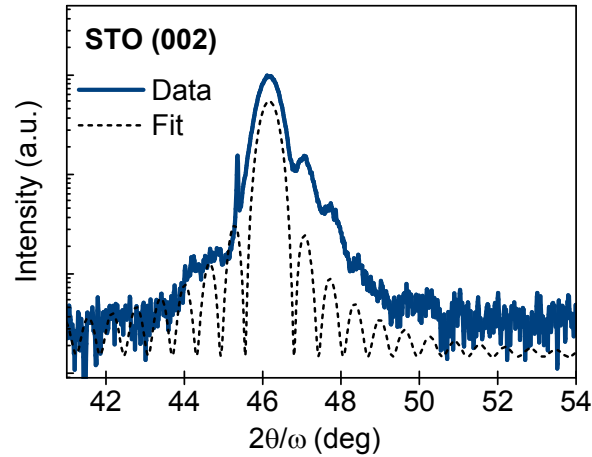
Supplementary Figure 3. X-ray diffraction of the (002) Bragg peak of epitaxial SrTiO$_3$ on GaAs.
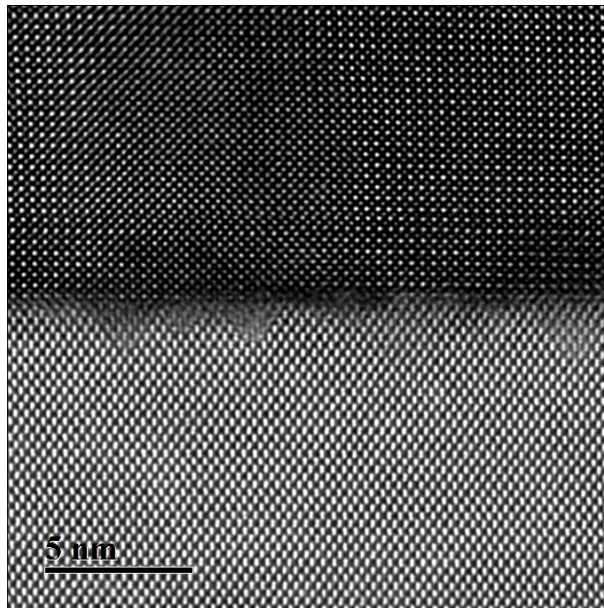
Supplementary Figure 4. Cross-section scanning-transmission electron microscope micrograph of the SrTiO$_3$/n-GaAs(001) interface acquired using high-angle annular dark-field imaging. This micrograph complements Fig. 1b by showing defects that are suspected to be caused by the electron beam in the microscope. The scale bar corresponds to 5 nm.
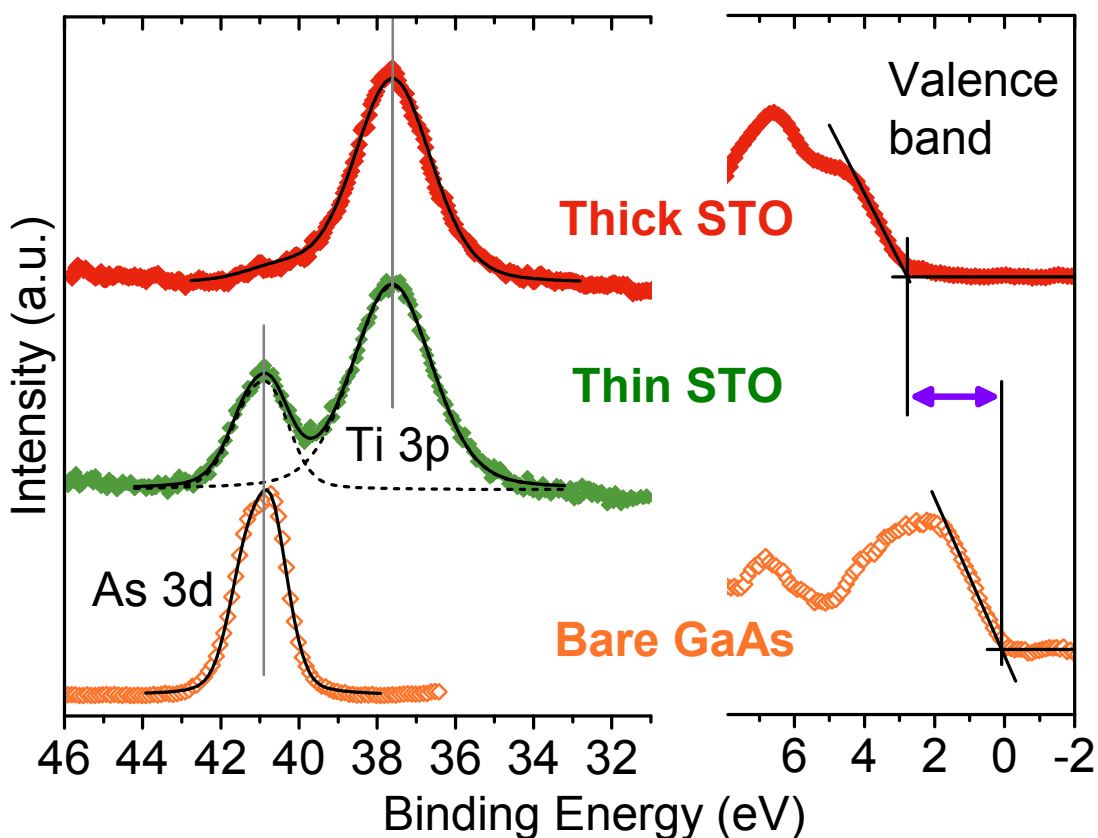
Electronic band structure at the oxide-semiconductor interface: spectroscopic analysis of the SrTiO$_3$-GaAs interface

The band alignment (Figs 1c and 1d) is measured[28,29,44,45] using x-ray photoemission spectroscopy (XPS) performed with non-monochromated Mg K$_\alpha$ radiation (1253.6 eV) and a pass energy of 11.75 eV. Removal of the Mg K$_\alpha$ satellites[46] is performed. The spectra are fit using the

XPSPEAK4.1 software after Shirley background subtraction. The Ti 3p peaks are fit using a single s-peak, and the As 3d peaks are fit using a d-doublet with a spin-orbit split (SOS) value of 0.7 eV.

The XPS spectra presented in Supplementary Fig. 5 are acquired from three different structures: (1) a thin (4 nm) oxide on GaAs structure that allows photoelectrons from the $SrTiO_3$ and the GaAs to be collected, (2) a thick (12 nm) oxide on GaAs structure where the oxide signal dominates the spectrum, and (3) a pristine GaAs piece that undergoes thermal desorption of the arsenic cap inside the XPS chamber.

The analysis is similar to that previously described [28,45], resulting in a $SrTiO_3$ conduction band that is 0.7±0.2 eV lower than that of the semiconductor. These values are in good agreement with 0.6±0.1 eV reported by Liang and co-workers.[47]


Supplementary Figure 5. Band structure analysis of the oxide-semiconductor interface. XPS spectra of the As 3d, Ti 3p and the valence band of thick and thin $SrTiO_3$/GaAs structure and of a clean GaAs interface.

Electronic structure at the oxide-electrolyte interface: Mott-Schottky analysis of Nb:SrTiO$_3$

A 1(at)% Nb-doped $SrTiO_3$ (100) single crystal electrode (Nb:STO) is prepared as follows: a 10x5 mm^2 piece of Nb:STO crystal (Princeton Scientific Corp.) is back-contacted with a titanium wire by painting small drops of a colloidal silver paint (Electron Microscope Science) and a liquid InGa eutectic (Sigma Aldrich). After drying, the edges and the back of the electrode are then covered with non-conductive epoxy (Omegabond 101, Omega) to prevent contact with the solution. The exposed front surface of the electrode is measured to be 0.094 cm^2.

Electrochemical impedance spectroscopy on the Nb:STO is performed by scanning the frequency in the range 0.1/1 Hz – $10^4/10^5$ Hz under the same experimental conditions as the STOPC samples: argon-saturated 0.1 M phosphate buffer pH 7, Ag/AgCl reference electrode and a Pt counter electrode (Supplementary Figs 6a-c). Data is acquired with both a Biologic SP300 and an EG&G 263A potentiostat coupled with a Solartron 1260 frequency response analyzer and analyzed with circuit fitting using both Zfit (ECLab) and ZView software (Scribner Associates). The equivalent circuit used to fit the experimental data is shown in the inset of Supplementary Fig. 6a, where the constant phase element (CPE_1) combines both the capacitance of the Helmholtz double-layer and of the depletion layer within the semiconductor. Data fitting provides a good estimation of the solution resistance ($R_1 = 108\Omega$ dark, $R_1 = 111\Omega$ under AM 1.5g). The values are then used for iR-correction of the Nb:STO cyclic voltammetry measurements (Fig. 2a).
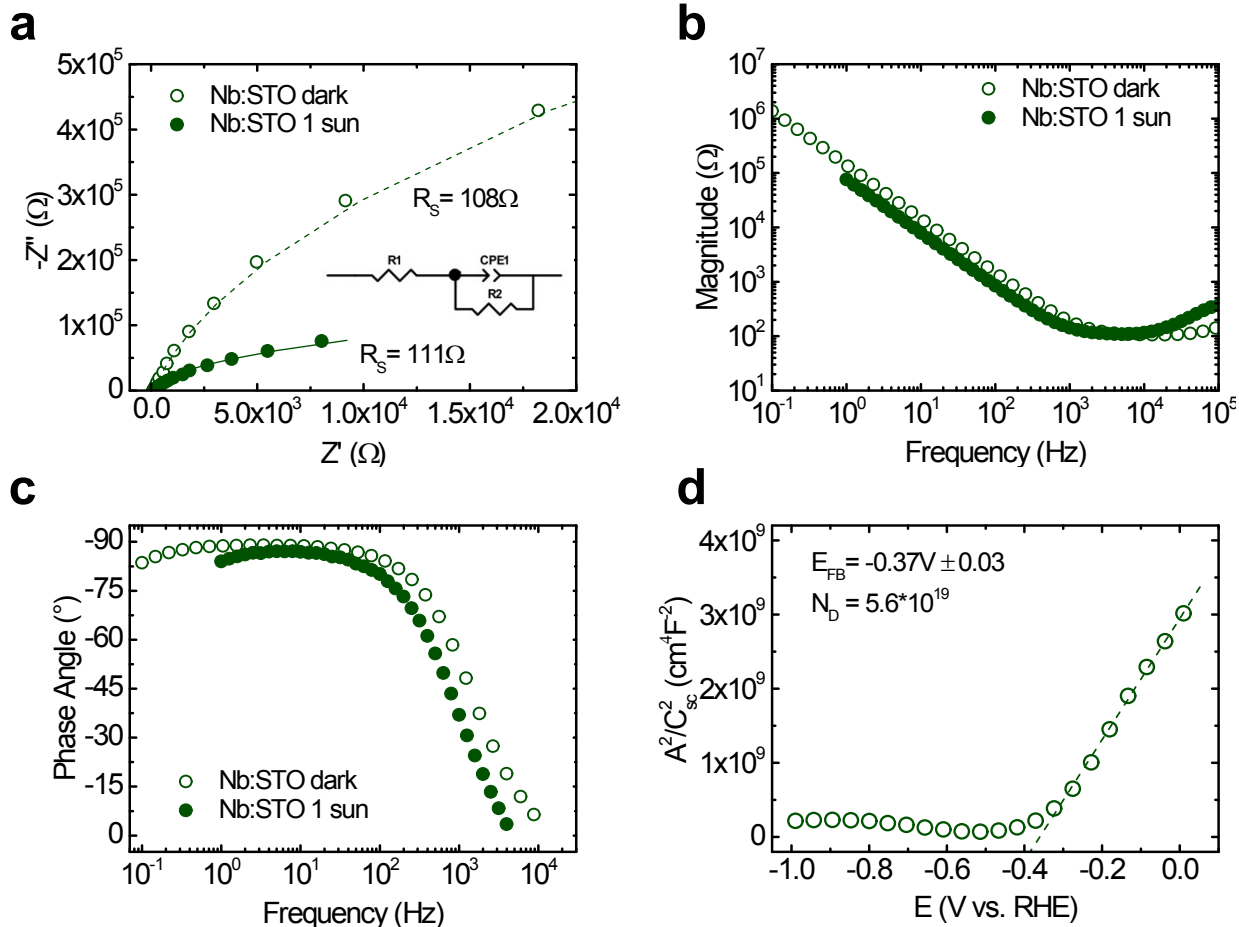
Supplementary Figure 6. Electrochemical impedance spectroscopy of 1(at)% Nb:STO at open circuit voltage in the dark and under 1 sun illumination. **a**, Nyquist plot of the impedance, **b**, Magnitude vs frequency ,**c**, Phase angle versus frequency and **d**, Mott-Schottky plot extracted from the impedance data for Nb:STO in 0.1M phosphate buffer. Fitting the linear portion of the curve yields a flat-band potential of -0.37±0.1 V_{RHE}. The estimated donor density is 5.6×10^{19} cm^{-3}.

To estimate the offset between the SrTiO$_3$ conduction band edge and the hydrogen redox level in the electrolyte, stepped potential electrochemical impedance spectroscopy is performed to enable Mott-Schottky analysis[48] for extraction of the flat-band potential. Applying an appropriate voltage, i.e. the flat-band potential, we can flatten the Nb:STO bands, obtaining the energy level of the conduction band.[49] By using a bulk Nb:STO crystal (0.5mm-thick), we can adopt with confidence the Mott-Schottky model to analyze the behavior of the surface capacitance (C_{SC}) as a function of the applied potential (E):

$$\frac{1}{C_{SC}^2} = \frac{2}{\varepsilon\varepsilon_0 N_D}\left(E - E_{fb} - \frac{k_B T}{e}\right).$$

A Mott-Schottky plot is acquired from 0 V to -1 V_{RHE} at a fixed frequency of 1.8kHz (Supplementary Fig. 6d). To estimate the donor density (N_D), a dielectric constant (ε) of 310,[50] and a surface area of 0.094cm^2 are used, yielding $N_D \sim 6 \times 10^{19}$ cm^{-3} from the slope of the fit, in good agreement with reported values.[51] By fitting the potential-dependent linear region, we extract a flat band potential (E_{FB}) of -0.37±0.1 V_{RHE} in the phosphate buffer. This value is slightly less negative than values measured in alkaline 0.1 M KOH[52] and thus more favorable for allowing photogenerated electrons to perform efficient hydrogen evolution.

This analysis assumes that the energetic offset of the Nb:STO with the electrolyte approximates the offset at the surface of the epitaxial SrTiO$_3$/GaAs photoelectrode. Conducting Nb-doped SrTiO$_3$ is required to pass measurable current through the bulk crystal and it further provides a model semiconductor-electrolyte Schottky junction for Mott-Schottky analysis. From the E_{FB} of -0.37±0.1 V_{RHE} we thus approximate the band alignment at the oxide-electrolyte interface, noting that a large overpotential (~370 mV) is generated in our device under operation resulting in high hydrogen evolution currents under 1-sun illumination.

Photoelectrochemical measurements

Three-electrode photoelectrochemical and dark electrochemical measurements are conducted using an Ag/AgCl reference electrode and a Pt mesh electrode in a glass cell with flat optical quartz end faces.[53] The working electrode contact is connected to the GaAs substrate back contact of the SrTiO$_3$/GaAs device; an InGa eutectic is scratched on the GaAs substrate, and then a titanium wire is attached with silver paint. The back, sides, and wire are covered with a nonconductive epoxy (Omegabond 101, Omega) so that only the SrTiO$_3$ layer is exposed to the electrolyte. Neutral 0.1 M potassium phosphate buffer (pH 7) in 18.2 MΩ deionized water is used as the electrolyte.[32] Current is passed through the cell via electron transfer from the SrTiO$_3$-GaAs to the electrolyte, resulting in hydrogen evolution (Figs 2a and 2b).

Since contaminants such as Fe can affect the catalytic properties of surfaces,[54] the following steps are implemented to rule out such effects: (i) Reagent-grade chemicals are used, (ii) CA measurements of STO-GaAs at $0V_{RHE}$ under 1 sun on a purified electrolyte (galvanostatic 12 hr electrolysis with sacrificial electrodes) are performed and show the same increase of current during the first hours, excluding the possible contribution of catalytic metals or other contaminants. (iii) XPS surveys acquired before and after long PEC operation are compared (Supplementary Fig. 8) and no new species are observable. Further investigation also rules out the catalytic effect of Pt contaminants under the described PEC conditions described in the main text (Supplementary Fig. 10-13)

Prior to PEC measurements, the electrochemical cell is purged with argon gas for 30 minutes. Argon is flowed through the PEC cell at 10 mL/min with the exhaust stream from the cell plumbed

directly into the gas chromatography system's sampling loop. The pressure in the PEC cell is ~2 psig during measurement. Photoelectrochemical measurements, including cyclic voltammetry, chronoamperometry and incident photon-to-current efficiency (IPCE) are performed with an EG&G 263A potentiostat.

A 300W Xe arc lamp is used to provide illumination. A Schott glass AM1.5g filter is used to produce simulated sunlight with the intensity calibrated with a c-Si Photovoltaic reference cell (SI BK-7, PV Measurements).

Cyclic Voltammetry (CV)

All cyclic voltammetry measurements (Fig. 2a) are performed at a scan rate of 10 mV s^{-1}. The iR correction is calculated using a solution resistance of 38Ω, which is determined from electrochemical impedance spectroscopy measurements (Biologic SP300) on a Pt wire working electrode. The Pt wire is cleaned with 37% HCl (Sigma-Aldrich) and rinsed with deionized (DI) water prior to measurements. Electrochemical impedance spectroscopy (EIS) measurements are conducted using 0.1 M potassium phosphate buffer with and without stirring at 500 rpm using a 2 cm stir bar, and identical solution resistances are measured for both conditions. In general, the ICPE improves after extended chronoamperometry (CA); this behavior is consistent with the activation seen comparing CV before and after CA (Supplementary Fig. 7).
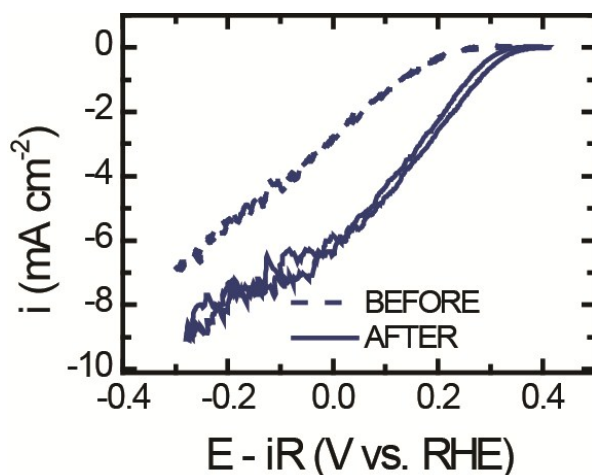
Supplementary Figure 7. The effect of extended electrolysis on the electrochemical characteristics of the photocathode. iR-corrected ($R_S = 38\Omega$) cyclic voltammetry (10 mV/s, 5th cycle) of SrTiO$_3$-GaAs photocathode (STOPC) in 0.1 M phosphate buffer with argon bubbling without stirring under simulated AM1.5g light before and after extended (>18 hr) electrolysis at 0 V$_{RHE}$.

Chronoamperometry (CA) and Gas Chromatography

During the chronoamperometry measurements (Fig. 2b), a 2 cm stir bar is rotated at 500 rpm to agitate the solution and reduce bubble accumulation on the surface. Hydrogen gas production is measured using gas chromatography (SRI GC 3610C in the multi-gas #3 configuration with a thermal conductivity detector (TCD) and a 6' S.S. Molecular Sieve 13X Packed Column) with argon carrier gas. Every 12 min, a sample is injected from the 1 mL sampling loop onto the column. A 5% H_2/N_2 gas mixture is used to calibrate the H_2 signal from the TCD.

Spectral response of the PEC performance: Incident Photon-to-Current Efficiency (IPCE)

For single-wavelength incident photon-to-current efficiency (IPCE) measurements of PEC performance (Figs 3a and 3b), the light from the Xe lamp is mechanically chopped at 30 Hz and coupled to a holographic grating monochromator (Newport Oriel). The current response as a function of bias is measured with the photocurrent being identified using a Merlin lock-in amplifier (Newport Oriel).

Photovoltaic "Dry" ICPE

ICPE for the dry solar cell structures (Fig. 3b) is measured in a PV Measurements Inc. QEX7, while current-voltage measurements are performed under a simulated AM1.5g spectrum using an ABET 10500 solar simulator.

Oxide stability during PEC operation

The stability of the oxide layer during PEC operation is of crucial importance for the feasibility of this approach as a sustainable energy source. To assess the endurance and integrity of the $SrTiO_3$ layer, XPS measurements are performed on the surface of the photocathode before and after PEC characterization, which includes CV, 24 hrs of CA, ICPE measurements, and CV again (Figs 2 and 3). The XPS measurements are conducted with Al Kα radiation (1486.7 ev) and a pass energy of 23.5 eV. Peak fitting is done using XPSPEAK4.1 after Shirley background subtraction.

A comparison of XPS surveys before and after PEC operation (Supplementary Fig. 8a) demonstrates that the surveys are similar and no significant changes to the $SrTiO_3$ are observed with following PEC operation.
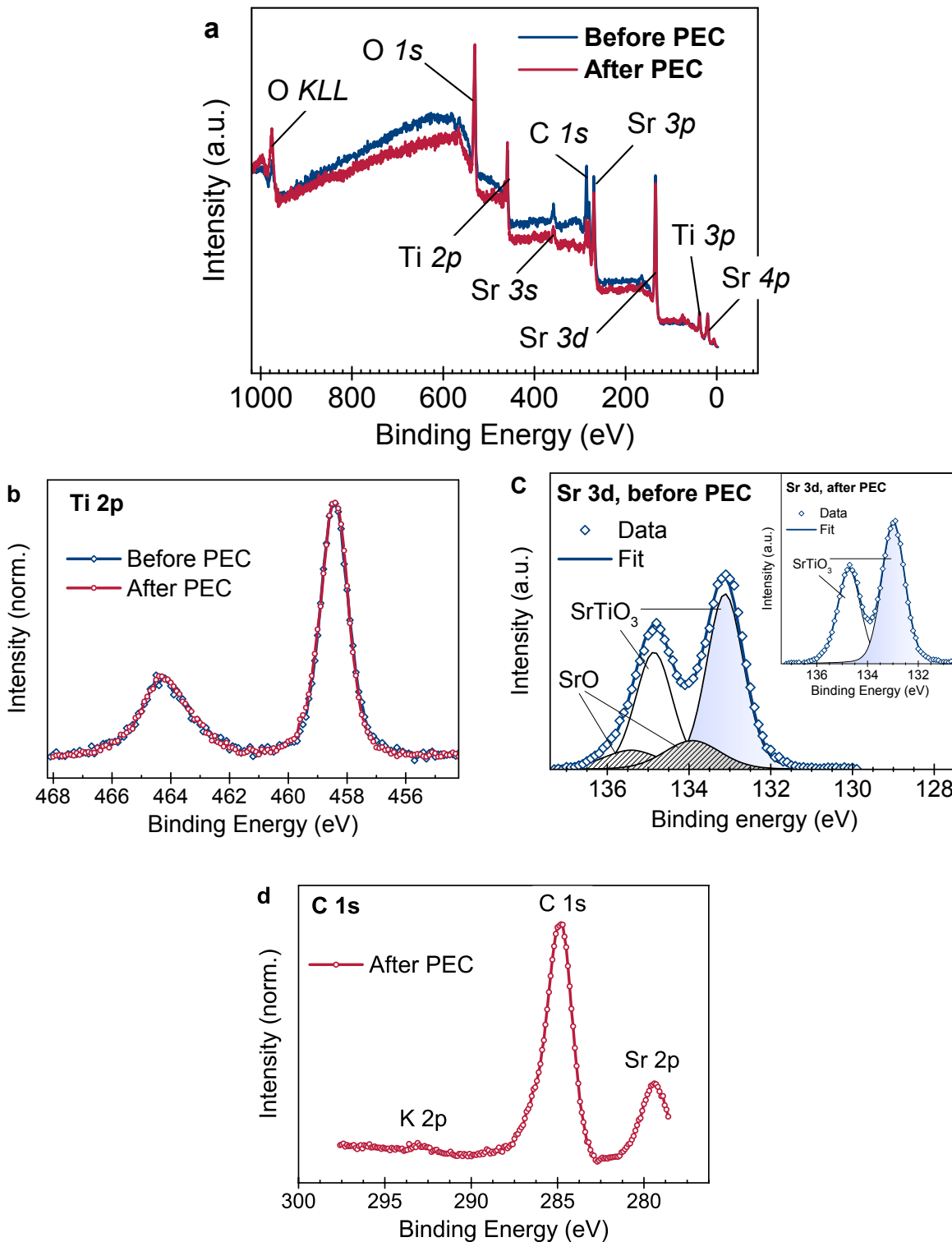
Supplementary Figure 8. XPS analysis of the SrTiO₃ surface before and after PEC of STOPC. Comparison between the before and after PEC of **a**, survey scans, **b**, Ti 2p and **c**, Sr 3d orbitals. **d,** K 2p scan after 24hr electrolysis at 0V RHE.

The Ti 2p peaks shown in Supplementary Fig. 8b exhibit identical spectra before and after PEC. This peak is sensitive to chemical state of Ti, and it displays a 4+ valence as expected for SrTiO$_3$[55] with no other states observable within the experimental resolution of XPS. To aid comparison of the peak shape, the data in Supplementary Fig. 8b is scaled so that energy of both peaks are at the same height, and the binding energy (BE) is aligned such as that the Ti 2p$_{3/2}$ components of both spectra are at 458.4 eV[56] to compensate for possible charging.

In contrast to the Ti data, the Sr 3d spectra (Supplementary Figure 8c) show a clear difference in the chemical state before and after 24 hr CA measurements (Fig. 2b). The Sr spectrum after PEC operation is fitted with a single chemical state of Sr in SrTiO$_3$, consisting of a d doublet with a spin-orbit split (SOS) value of 1.74 eV while that before PEC operation includes a minor component of SrO, a possible consequence of small excess in the Sr flux during growth. Indeed, similar Sr 3d spectra are reported by Szot et al.[57] for SrO on SrTiO$_3$. To verify this interpretation, the 'before' spectrum (Supplementary Figure 8c) is fitted using the same doublet as the one used in the 'after' spectrum (inset), and an additional d doublet with an SOS value of 1.5 eV and a BE shift of +0.8 eV relative to the SrTiO$_3$ component, which are the same parameters previously reported.[57] The resulting fit shows excellent agreement to the data, illustrating that the pristine PEC cells contain a small amount of SrO on the surface initially. The SrTiO$_3$ is unaffected by the photoelectrochemical hydrogen production. Based on these observations, we propose the SrO dissolution during the initial scale as a probable source for the ~2 hr activation time in the CA data (Fig. 2b). Chemical changes to the surfaces of similar catalysts have been suggested in the literature, such as Sr leaching out of SrIrO$_3$ catalyst,[58] and structural modifications to SrTiO$_3$ surfaces.[59]

XPS after 24hr electrolysis at 0 V RHE shown in Supplementary Fig. 8d demonstrates the presence of trace amounts of potassium, with the observation of the largest potassium peak at ~293 eV, supporting that the presence of particles can be attributed to trace electrolyte salts, as shown in Supplementary Figure 9d.

Scanning Electron Microscopy (SEM)

SEM images are taken with a Zeiss Merlin high-resolution SEM and ultra-high resolution Supra VP SEM. Supplementary Fig. 9 shows SEM images of bare GaAs electrodes before (Supplementary Fig. 9a) and after 4 hrs of electrolysis at 0 V$_{RHE}$ (Supplementary Fig. 9b). The importance of protecting the GaAs is highlighted by Supp. Fig. 9b, showing catastrophic damage to the semiconductor under short operating times. Therefore, as long as the SrTiO$_3$ film is completely *continuous*, we do not expect degradation of the underlying GaAs. However, the importance of single crystallinity of the oxide is highlighted by low-loss transport of photogenerated electrons across the GaAs-oxide interface, e.g. Fig. 3b, showing the same IPCE values for cells with and without the oxide. We ascribe this loss-less transport to the high degree

of order at the interface (Fig. 1b). We believe that obtaining such an ordered interface may prove challenging using non-epitaxial oxide deposition techniques. Corrosion of the bare GaAs upon photoelectrolysis is severe. In contrast, the STOPC photocathode shows no evidence of corrosion after 24 hours of photoelectrochemical hydrogen evolution (Supplementary Fig. 9c before and 9d after).
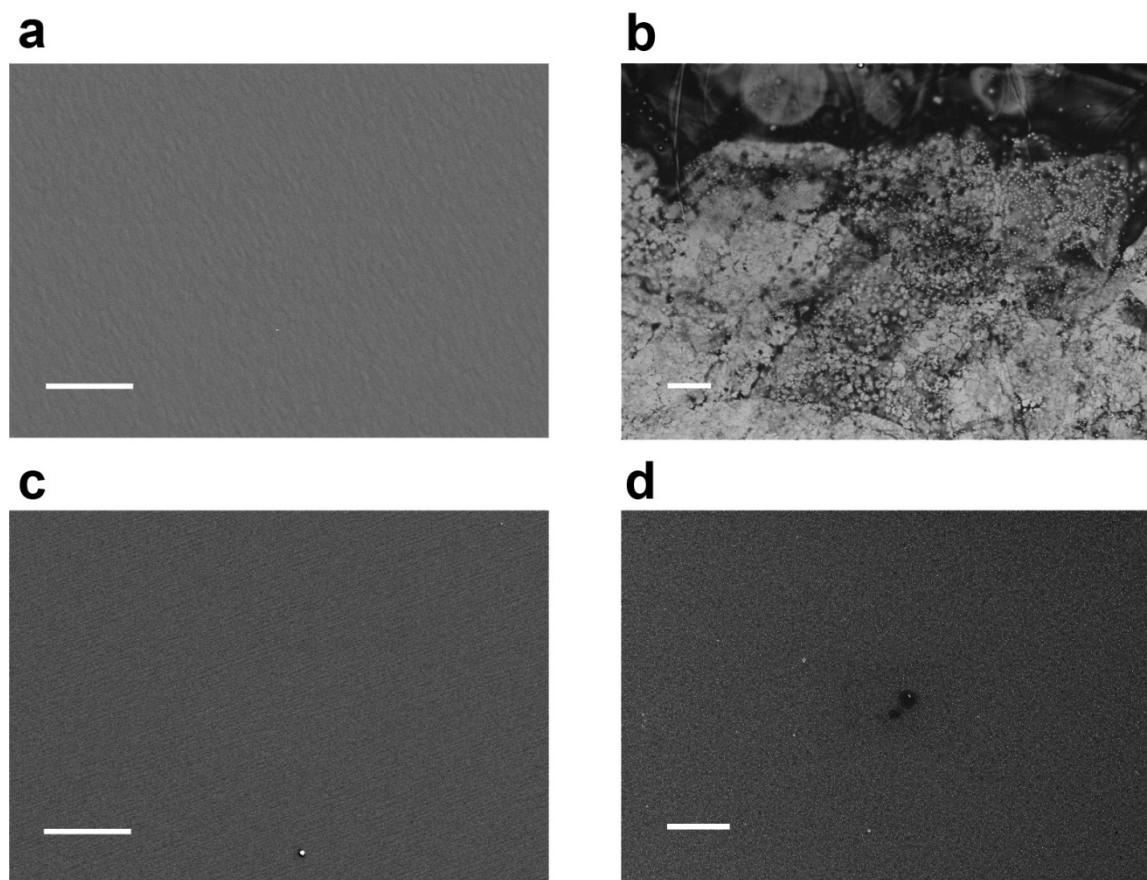
Supplementary Figure 9. Morphological analysis of the surface stability of the photocathodes. Scanning electron microscope images of **a**, the bare solar cell wafer (Supplementary Table 1) before any electrochemistry (scale bar, 5 μm) and **b**, after photoelectrochemistry (scale bar, 20 μm).**c**, The STOPC surface before (scale bar, 5 μm) and **d**, after photoelectrochemistry (scale bar, 5 μm). Particles observed after electrochemical measurements in Panels b and d, are attributed to trace residual electrolyte salts.

Trace metal impurities analysis

In order to rule out the possibility of trace metal impurities, such as platinum, impacting the catalytic performance of the photocathode device during PEC, a combined PEC and XPS study was conducted. All PEC measurements were conducted under Ar bubbling, with stir bar rotation at 500 rpm, and with an Ag/AgCl reference electrode. All CVs were measured with a 10 mV s^{-1} scan rate and shown without iR compensation.

The PEC activity of a STO-GaAs photocathode device was assessed with CVs prior to and after long-term electrolysis. Several precautions were taken to avoid the introduction of contaminants, especially Pt, throughout the course of PEC that might contribute to the catalytic activity of the photocathode device: (i) use of a high-purity potassium phosphate buffer solution (> 99.995% monobasic, > 99.999% dibasic) (ii) cleaning of the PEC glassware by aqua regia prior to photoelectrochemical experiments (iii) use of a graphite rod (Pine Electronics) counter electrode. The CVs and 24 hr chronoamperometry (CA) in Fig. S10 compare the STO-GaAs activity prior to and after long-term CA at 0 V RHE under the "Pt-free" setup, where the current or activity was increased similarly (referred to as "activation") to the results presented in Fig. 2b where Pt counter electrode was employed. XPS measurements taken after long-term CA confirmed the absence of Pt deposition on the surface throughout the course of the PEC experiments. Survey scans and the Pt 4f regional scan show no first row transition metal peaks (600-1000 eV BE) nor Pt 4f peaks (~71 eV) detected on the STO surface, respectively (Fig. S11).

We further show that having Pt presence on the STO surface obtained from CA measurements using Pt counter electrode did not lead to noticeable increase in the current or activity (Figure S12 and S13). We conducted a series of experiments to determine the effect of Pt dissolution from the counter electrode on the photocathode activity, namely whether the possibility of Pt deposition onto the STO surface is responsible for the photocathode activity enhancement observed in Figure 2b (main text). To investigate this possible mechanism, we conducted a well-controlled experiment immediately after the PEC experiments shown in Fig. S10 and S11 in an effort to intentionally dissolve Pt from the counter electrode into the electrochemical setup. The graphite rod counter electrode was removed and replaced with a bare Pt counter electrode directly exposed to the PB electrolyte, and then long-term CA was conducted at 0 V RHE. CVs taken before and after the CA do not exhibit discernable increase in activity after the intentional Pt operation (Fig. S12). Additionally, survey and Pt 4f XPS scans of the STO surface after this CA show noticeable appearance of the strong Pt 4f 7/2 peak (Fig. S13), indicating some Pt deposition onto the STO surface. Combined, the CV and XPS results demonstrate that even with evidence of Pt deposition on the STO surface, no observable change in the electrocatalytic activity of the device occurred after extended CA.

Therefore, the PEC and XPS results in conjunction strongly support that the bare STO surface is intrinsically electrocatalytically active for HER after an activation process and rule out that the activity can be attributed to Pt contamination on STO in the electrochemical performance of the photocathodes. The HER activity and changes in reactivity over the course of CA are in agreement with previous studies of the STO surface[58] albeit under slightly different PEC conditions.
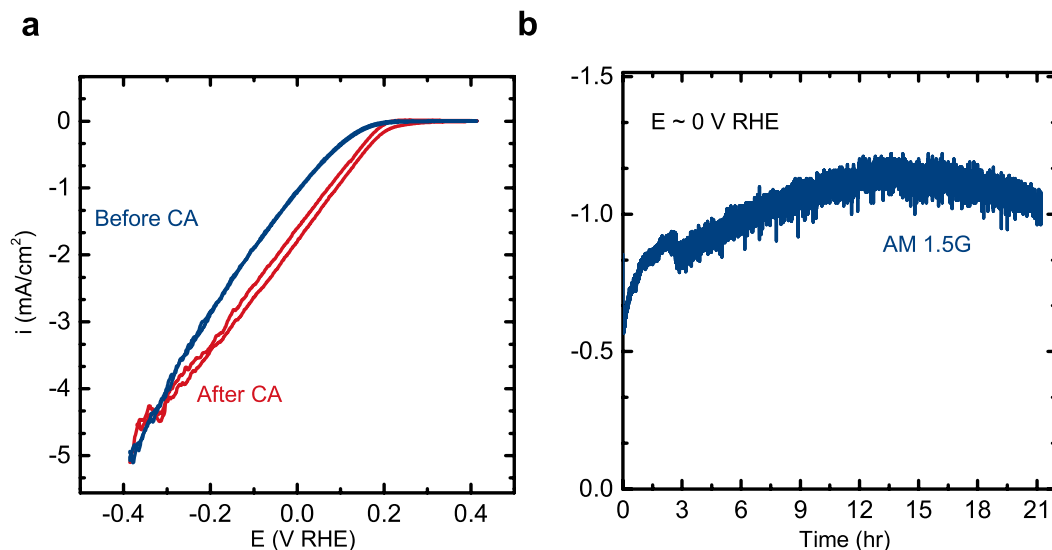

Supplementary Figure 10. a, CVs conducted before and after long-term potentiostatic tests at E ~ 0 V RHE under AM1.5G solar illumination. Improvement in the onset potential is observed. **b**, Long-term potentiostatic measurements at E ~ 0 V RHE under AM1.5G illumination.
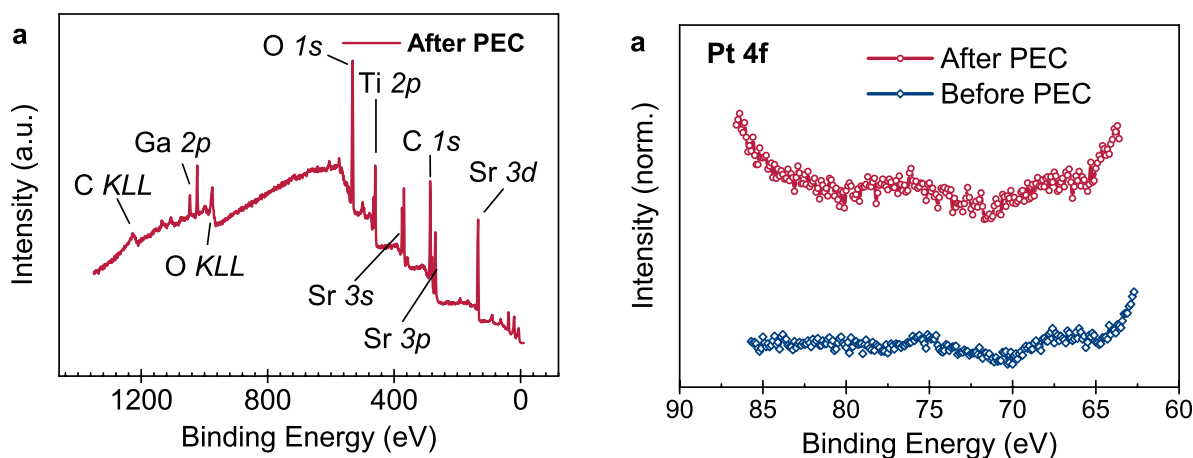
Supplementary Figure 11. a, Survey scan of the STO-GaAs device after the long-term CA shown in Supplementary Fig. 10. **b**, High-resolution Pt 4f scan region indicate no appearance of the Pt 4f 7/2 peak at ~72 eV.
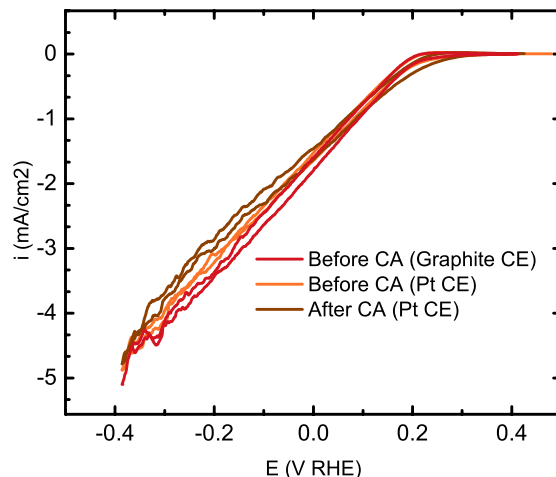
Supplementary Figure 12. The effect of Pt contaminants introduced from the counter electrode (CE) on the electrochemical performance of the photocathode. CV measurements under AM1.5G illumination after long-term CA with the "Pt-free setup" (red), after the graphite rod counter electrode was replaced with a bare exposed Pt wire counter electrode (orange), and after long-term CA with the exposed Pt wire counter electrode (brown).
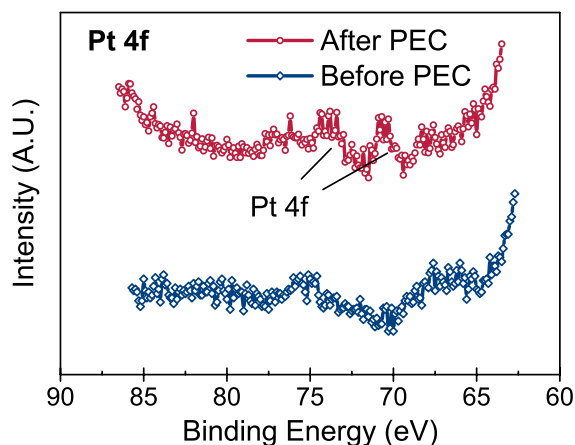
Supplementary Figure 13. High-resolution XPS scans of the Pt 4f region for the pristine STO-GaAs device (blue) and the device after CA with the exposed Pt CE where Pt was intentionally deposited onto the STO surface (brown). Spectra are normalized and offset for ease of clarity. Appearance of the strong Pt 4f 7/2 peak at ~71 eV as well as the corresponding doublet peak at ~74 eV is observed.

## Dry photovoltaic cell characteristics with SrTiO$_3$ layer

The dry, lighted J-V curves for np GaAs solar cells with and without STO are presented in Supplementary Fig. 10. The layer structure of the GaAs junction is identical in all cases, and the work function of the metal on the STO was slightly varied from ~4.3 eV to ~4.5 eV through the use of Al and Cr electrodes, respectively. The non-linearity of the metal/STO/n-GaAs junctions manifests itself as an S-shaped J-V curve under illumination.[60] An energetic barrier exists between the STO and n-GaAs (manuscript Fig. 1c), and this energetic barrier causes the red and green curves in Supplementary Fig. 10 to reach lower V_{oc} values than the black curve. These data sets show that the photoelectrode is rather resistive, and we suggest that the STO essentially serves as a lossy, electron-selective contact.
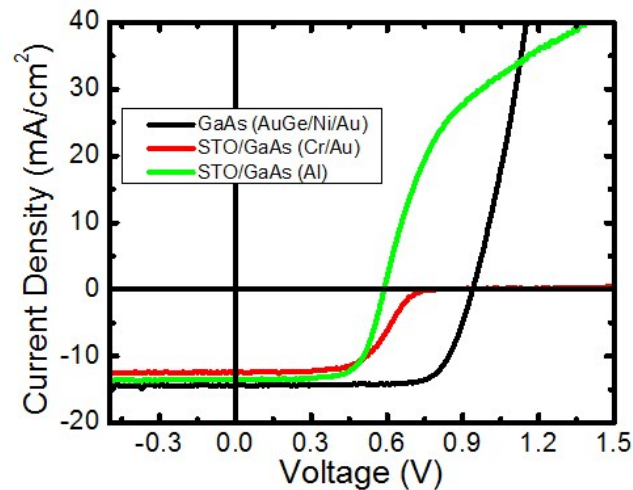
Supplementary Figure 14. Dry, lighted (~AM1.5G) J-V characteristics of GaAs solar cell without STO (black), Au/Cr/STO/GaAs solar cell (red), and Al/STO/GaAs solar cell (green). The STO introduces a strongly non-linear element in series with the GaAs solar cell, leading to the "S-shaped" characteristics.[60]

19

The concept of 'implied V_{oc}', representing the quasi-Fermi level (QFL) splitting within the GaAs under illumination (Supplementary Fig. 1b), is useful in explaining the reduced V_{oc} observed when STO is grown on the cell.[61] The black curve, where low-resistance ohmic contacts are formed on the solar cell, yields the maximum V_{oc} of 0.95 V that can be expected for this unpassivated device under 1-sun (Supplementary Fig. 10). In this case, the volt-meter is in direct communication with the QFLs of the semiconductor, and no significant voltage drop occurs across the contacts. 0.95 V can then be used as the implied V_{oc} for the green and red curves of Supplementary Fig. 10. The addition of STO on top of the GaAs solar cell incurs upward band-bending of the n^+GaAs cathode (manuscript Fig. 1c), which leads to an open-circuit voltage loss ΔV_{oc}. In this case, the volt-meter observes a reduced voltage of 0.95 V$- \Delta V_{oc}$, where the value of ΔV_{oc} is dependent on the band-bending within the STO/n-GaAs and the illumination conditions. The exact band-bending at the STO/n-GaAs junction depends on a number of independently quantifiable factors including: interface state density, doping of the STO, metal electrode work-function, and the presence/absence of external bias, which itself depends on illumination conditions and operating point. The effect of the metal work-function on ΔV_{oc} can be varied by changing the metal, as illustrated by the green and red curves in Supplementary Fig. 10 with measured V_{oc} values of 0.6 and 0.75 V, respectively. In general, discrepancies in implied V_{oc} and measured V_{oc} are common and have been explored previously in InP solar cells coated with TiO_2, ITO, and CdS.[62] Clearly, an ideal electron-selective contact would have $\Delta V_{oc} = 0$.

From a circuit standpoint, the metal/STO/n-GaAs junction can be approximated as a leaky Schottky diode in series with a resistor that blocks electrons from exiting the n^+GaAs while developing a photovoltage that opposes the np GaAs junction;[60] the magnitude of this non-ideal photovoltage is ΔV_{oc} (0.35 V for Al/STO and 0.2 V for Au/Cr/STO). The Au/Cr/STO/n-GaAs junction is more strongly blocking than the Al/STO/n-GaAs junction, as indicated by the fact that the red curve in Supplementary Fig. 11 fails to flow any forward current, even at 1.5 V forward bias.
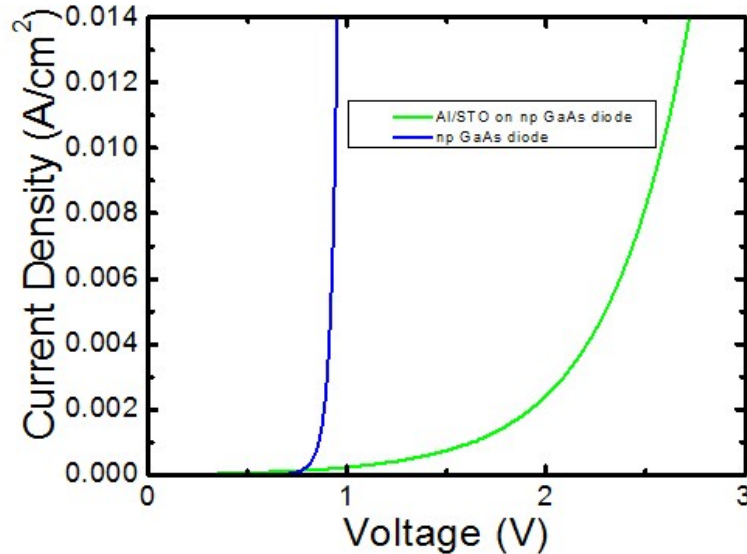
Supplementary Figure 15. Dark I-V characteristics of np GaAs diode and Al/STO on np GaAs diode. High forward voltage is needed to force current injection when the Al/STO is present.

The blocking effect of the Al/STO on GaAs can also be seen without external illumination, where the np GaAs junction operates as a light-emitting diode. As Supplementary Fig. 11 shows, to reach a given forward current, the Al/STO-coated np GaAs diode must drop an additional 1.0-1.5 V compared to the np GaAs diode; higher current levels require even more voltage, a signature of a non-ideal device. Furthermore, the non-linear effects lead to a breaking of the superposition assumption that normally applies to well-behaved solar cells.[63] Supplementary Fig. 10 shows that J_{sc} of the GaAs solar cell is ~14 mA/cm^2. The dark GaAs diode in Supplementary Fig. 11 takes ~0.95 V to reach 14 mA/cm^2, which is the exact bias or QFL splitting required to cancel the photocurrent (i.e. V_{oc}), in accordance with superposition. In contrast the Al/STO/GaAs diode takes >2.5 V to reach its J_{sc} of ~14 mA/cm^2 in the dark, while its V_{oc} is only 0.6 V. The Al/STO/GaAs diode does not conform to the superposition assumption, and appears to have rich bias and light-dependent behaviors.

In conclusion, the dark and lighted J-V curves presented here show that illumination-dependent non-linearities exist in these 'dry' devices, and provide a qualitative indication of energy loss that occur in the 'wet' devices. More efficient solar-to-hydrogen conversion is accessible via STO/GaAs interface engineering, towards improving the oxide's performance as an electron-selective contact. Routes for achieving these improvements include n-doping of the epitaxial STO, and engineering of band offsets with GaAs by alloying of the oxide.

Supplementary references

39   A. Luque and S. Hegedus, *Handbook of Photovoltaic Science and Engineering*, Wiley, 2003.

40   S. M. Sze and K. K. Ng, *The Physics of Semiconductor Devices*, Wiley, 3rd edn., 2007.

41   R. Droopad, R. Contreras-Guerrero, J. P. Veazey, Q. Qiao, R. F. Klie and J. Levy, *Microelectron. Eng.*, 2013, **109**, 290–293.

42   Y. Liang, J. Kulik, T. C. Eschrich, R. Droopad, Z. Yu and P. Maniar, *Appl. Phys. Lett.*, 2004, **85**, 085905.

43   A.-B. Posadas, M. Lippmaa, F. J. Walker, M. Dawber, C. H. Ahn and J.-M. Triscone, in *Physics of Ferroelectrics*, Springer Berlin Heidelberg, Berlin, Heidelberg, 2007, vol. 105, pp. 219–304.

44   E. A. Kraut, R. W. Grant, J. R. Waldrop and S. P. Kowalczyk, *Phys. Rev. Lett.*, 1980, **44**, 1620–1623.

45   L. Kornblum, M. D. Morales-Acosta, E. N. Jin, C. H. Ahn and F. J. Walker, *Adv. Mater. Interfaces*, 2015, **2**, 201500193.

46   C. D. Wagner and G. E. Muilenberg, *Handbook of X-ray photoelectron spectroscopy*, Perkin-Elmer, 1979.

47   Y. Liang, J. Curless and D. McCready, *Appl. Phys. Lett.*, 2005, **86**, 082905.

48   A. J. Bard and L. R. Faulkner, *Electrochemical Methods: Fundamentals and Applications*, Wiley, 2nd edn., 2001.

49   S. R. Morrison, *Electrochemistry at Semiconductor and Oxidized Metal Electrodes*, Plenum Press, New York, 1980.

50   G. Rupprecht and R. O. Bell, *Phys. Rev.*, 1964, **135**, A748–A752.

51   T. Watanabe, A. Fujishima and K. Honda, *Bull. Chem. Soc. Jpn.*, 1976, **49**, 355–358.

52   T. Ming, J. Suntivich, K. J. May, K. A. Stoerzinger, D. H. Kim and Y. Shao-Horn, *J. Phys. Chem. C*, 2013, **117**, 15532–15539.

53   W. Hong, M. Risch, K. A. Stoerzinger, A. J. L. Grimaud, J. Suntivich and Y. Shao-Horn, *Energy Environ. Sci.*, 2015, **8**, 1404–1427.

54   L. Trotochaud, S. L. Young, J. K. Ranney and S. W. Boettcher, *J. Am. Chem. Soc.*, 2014, **136**, 6744–6753.

55   M. S. J. Marshall, D. T. Newell, D. J. Payne, R. G. Egdell and M. R. Castell, *Phys. Rev. B*, 2011, **83**, 35410.

56   R. T. Haasch, E. Breckenfeld and L. W. Martin, *Surf. Sci. Spectra*, 2014, **21**, 87.

57   K. Szot, W. Speier, U. Breuer, R. Meyer, J. Szade and R. Waser, Surf. Sci., 2000, **460**, 112–128.

58   M. Plaza, X. Huang, J. Y. P. Ko, M. Shen, B. H. Simpson, J. Rodr'\iguez-López, N. L. Ritzert, K. Letchworth-Weaver, D. Gunceler, D. G. Schlom and others, J. Am. Chem. Soc., 2016, **138**, 7816–7819.

59   L. C. Seitz, C. F. Dickens, K. Nishio, Y. Hikita, J. Montoya, A. Doyle, C. Kirk, A. Vojvodic, H. Y. Hwang, J. K. Norskov and T. F. Jaramillo, Science, 2016, **353**, 1011–1014.

60   C. Battaglia, S. M. de Nicolás, S. De Wolf, X. Yin, M. Zheng, C. Ballif and A. Javey, *Appl. Phys. Lett.*, 2014, **104**, 113902.

61   M. Ghannam, Y. Abdulraheem and G. Shehada, *Sol. Energy Mater. Sol. Cells*, 2016, **145**, 423–431.

62   X. Yin, C. Battaglia, Y. Lin, K. Chen, M. Hettick, M. Zheng, C.-Y. Chen, D. Kiriya and A. Javey, *ACS Photonics*, 2014, **1**, 1245–1250.

63   S. J. Fonash, *Solar Cell Device Physics*, 2010.